Chemical Science

ROYAL SOCIETY OF CHEMISTRY

EDGE ARTICLE

View Article Online
View Journal | View Issue

Cite this: *Chem. Sci.*, 2025, **16**, 2429

All publication charges for this article have been paid for by the Royal Society of Chemistry

Received 24th September 2024
Accepted 23rd December 2024

DOI: 10.1039/d4sc06477a

rsc.li/chemical-science

Spin effects in regulating the adsorption characteristics of metal ions†

Cunyuan Gao,‡[a] Shiyu Zhen,‡[b] Yutong Wang,[a] Lingwei Wang,[a] Yang Cao,[a] Jinhua Zhan,[a] Liang Zhang *[bc] and Bin Cai *[ad]

Understanding the adsorption behavior of intermediates at interfaces is crucial for various heterogeneous systems, but less attention has been paid to metal species. This study investigates the manipulation of Co^{3+} spin states in $ZnCo_2O_4$ spinel oxides and establishes their impact on metal ion adsorption. Using electrochemical sensing as a metric, we reveal a quasi-linear relationship between the adsorption affinity of metal ions and the high-spin state fraction of Co^{3+} sites. Increasing the high-spin state of Co^{3+} shifts its d-band center downward relative to the Fermi level, thereby weakening metal ion adsorption and enhancing sensing performance. These findings demonstrate a spin-state-dependent mechanism for optimizing interactions with various metal species, including Cu^{2+}, Cd^{2+}, and Pb^{2+}. This work provides new insights into the physicochemical determinants of metal ion adsorption, paving the way for advanced sensing technologies and beyond.

Introduction

Adsorption and desorption of intermediates on solid surfaces are fundamental components in various heterogeneous systems, particularly in catalysis,[1,2] environmental science,[3,4] and materials engineering.[5,6] These processes are critical in understanding reaction pathways that occur at solid-involved interfaces and optimizing device efficiencies.[7,8] For instance, typical catalysis on solid surfaces consists of the adsorption of reactants, the chemical transformations of intermediates, and the desorption of products.[9] Based on these processes, the Sabatier principle demonstrates the importance of optimal catalyst surfaces that bind reactants neither too strongly nor too weakly.[10] This balance ensures sufficient interaction for the reaction to occur while allowing products to desorb efficiently, which indicates a primary strategy in catalyst design.[11–13] The subsequent development of d-band theory further enriches the catalysis toolbox by explaining how the electronic properties of catalysts affect their adsorption characteristics with adsorbates.[14–16] In addition, the impact of geometric properties for these processes has also been well studied, providing further guidance for the optimization of catalyst surfaces.[17,18] While understanding these behaviors is essential for the design of solid surfaces to improve heterogeneous systems, current research primarily focuses on non-metallic adsorbates (such as C,[19] H,[20] and O[21]), often overlooking their interaction with metal species.

Unveiling the physicochemical parameters that govern the adsorption and desorption processes of metal adsorbates at interfaces holds great promise in metallurgy,[22] metal-ion batteries,[23,24] and sensor technology.[25] Electrochemical sensing of metal ions involves adsorption, migration, electron transfer, and desorption processes of metal species at the electrochemical interface, enabling effective investigation of their interaction with solid interfaces.[26,27] However, research on the adsorption processes of metallic species, similar to that of the non-metallic adsorbates, is still limited in tuning the electronic structures through doping, morphology, crystal planes, and defects.[28,29] Recently, spin, an intrinsic property of electrons, has emerged as another promising degree of electronic freedom to regulate the electronic structure of various catalyst surfaces.[30–32] However, the spin state of active centers is influenced by splitting energy and electron pairing energy, making it challenging to directly modulate the spin state.[33] Consequently, the correlation between spin properties and adsorption characteristics of metal species remains largely unexplored.

Herein, we address this challenge by correlating the spin state of Co^{3+} sites with their adsorption characteristics for various metal ions, including Cu^{2+}, Cd^{2+}, and Pb^{2+} ions. Transition metal oxides are employed due to their strong interdependence between spin, charge, orbital, and lattice degrees of freedom, creating a highly interactive system for manipulating

[a]School of Chemistry and Chemical Engineering, Shandong University, 250100 Jinan, China. E-mail: bin.cai@sdu.edu.cn

[b]Center for Combustion Energy, School of Vehicle and Mobility, State Key Laboratory of Intelligent Green Vehicle and Mobility, Tsinghua University, Beijing 100084, China. E-mail: zhangbright@tsinghua.edu.cn

[c]Beijing Huairou Laboratory, Beijing 101400, China

[d]Shenzhen Research Institute of Shandong University, Shenzhen 518000, China

† Electronic supplementary information (ESI) available. See DOI: https://doi.org/10.1039/d4sc06477a

‡ These authors contributed equally.

spin states through various pathways.[34] Spinel oxide $ZnCo_2O_4$ is an ideal choice because Co^{3+} cations are confined to octahedral sites, allowing exclusive investigation of CoO_6 octahedra. The manipulation of the Co^{3+} spin state is achieved by calcination-induced lattice distortion, which is carefully verified through density functional theory (DFT) calculations, Fourier-transform infrared spectroscopy (FTIR), X-ray absorption spectra (XAS) and Superconducting Quantum Interference Device (SQUID) analysis. Increasing the calcination temperature leads to an increase in the spin state of Co^{3+} cations, causing the d-band center to shift downward relative to the Fermi level. The lower energy level of the d-band center results in the antibonding orbitals being occupied by more electrons, weakening the adsorption affinity between the Co^{3+} sites and metal ions. As the desorption process plays a major role in determining the sensing signal, weakened metal ion adsorption leads to enhanced sensing performances. This positive correlation between the spin state and sensing activity applies to various metal ions, including Cu^{2+}, Cd^{2+}, and Pb^{2+} ions. This work sheds light on the understanding of spin properties in optimizing the adsorption characteristics of metal species and would spur new strategies in optimizing electrochemical sensors by spin engineering.

Results and discussion

In the spinel oxide $ZnCo_2O_4$, Zn^{2+} and Co^{3+} cations occupy four-coordinated tetrahedral and six-coordinated octahedral sites, respectively (Fig. 1a). Zn^{2+} cations are considered inert with limited electrochemical activity due to their filled 3d orbital and lower electron affinity compared to other catalytically active 3d-transition metals. Therefore, the Co^{3+} sites in octahedral units play a dominant role during the electrochemical adsorption and desorption processes of metal ions.[27] The spin state of metals is determined by the crystal field splitting energy and electron pairing energy.[35] Due to the high crystal field splitting energy, Co^{3+} typically favors the low-spin state ($t_{2g}^6e_g^0$) in an octahedral geometry, where the t_{2g} orbitals are fully occupied and the e_g orbitals are completely empty (Fig. 1b). The empty e_g orbitals provide enormous opportunities for spin state engineering. As shown in Fig. 1b, the e_g orbitals can accommodate up to two unpaired electrons, resulting in the intermediate-spin state ($t_{2g}^5e_g^1$) and high-spin state ($t_{2g}^4e_g^2$), respectively. Thus, the electronic structure of Co^{3+} sites can be effectively regulated through spin engineering, resulting in significant changes in electrochemical activity.

A series of $ZnCo_2O_4$ spinel oxides with varied Co^{3+} spin states was obtained by tuning the calcination temperatures to induce lattice distortion during the sol–gel synthesis (*i.e.* 300, 400, 500, and 600 °C, denoted as ZCO-300, ZCO-400, ZCO-500, and ZCO-600, respectively). Current methods for controlling the spin state include lattice distortion,[36,37] defect engineering,[38,39] heteroatom doping,[40,41] and metal–carrier interaction.[42] Among these, the lattice distortion-induced method offers a more straightforward and scalable approach to modulate the volume proportion of high-spin Co^{3+}.[33] This facilitates the detailed exploration of the structure–activity relationship, which is critical for advancing spin-state-dependent applications. The as-obtained $ZnCo_2O_4$ oxides show irregular morphology according to transmission electron microscopy (TEM) characterization (Fig. S1†). Increasing calcination temperature leads to slight sintering and increased particle sizes. Fig. 1c and d show the aberration-corrected high angular annular dark-field scanning TEM (AC-HAADF-STEM) image and the corresponding fast Fourier transform (FFT) pattern of the ZCO-600 oxide. The atomic arrangement of ZCO-600 matches well the spinel lattice with the space group *Fd*3*m*, where Co^{3+} cations occupy the octahedral sites and Zn^{2+} cations occupy the tetrahedral sites.[43] As shown in Fig. 1e, the X-ray diffraction (XRD) analysis further confirms the successful synthesis of the spinel phase (JCPDS no. 23-1390) at different calcination temperatures. In particular, the main peaks located at about 31.21, 36.81, 59.28 and 65.15° are indexed as 220, 311, 511 and 440 Bragg reflections of the spinel crystal structure, respectively. This aligns with the space group *Fd*3*m*, and agrees well with the AC-HAADF-STEM analysis. No obvious diffraction peaks of impurities were observed within the calcination temperature range of 300 to 600 °C, indicating excellent structural robustness of the $ZnCo_2O_4$ spinel oxide.

Further analysis of the chemical and spin states of $ZnCo_2O_4$ spinel oxide was performed using X-ray photoelectron spectroscopy (XPS) and XAS (Fig. 1f and S2–S4†). The XPS analysis of the Co 2p signal (Fig. S3†) confirms that Co within all $ZnCo_2O_4$ spinel oxides exhibits a trivalent oxidation state. The Co L_2 and L_3 XAS spectra of $ZnCo_2O_4$ are presented in Fig. 1f, together with Co_2O_3 as a Co^{3+} reference. The center of the L_3 spectrum of $ZnCo_2O_4$ aligns with that of Co_2O_3, demonstrating that the Co valence in $ZnCo_2O_4$ is indeed trivalent. Previous studies have shown that the presence of a low-energy shoulder (red area) at the Co^{3+} L_3 edge is characteristic of the high-spin state,[44] while the high-energy shoulder (blue area) is indicative of the low-spin state.[45] This analysis proves that Co^{3+} cations in $ZnCo_2O_4$ exist predominantly in the high-spin state. Hence, the consistent trivalent oxidation state of Co ensures an exclusive examination of the spin-dependent electrochemical activity in $ZnCo_2O_4$ spinel oxide.

The emergence of the Co^{3+} high-spin state is ascribed to lattice distortion induced by high-temperature calcination. We explore the spin-structure correlation using both DFT calculations and FTIR characterization. Fig. 1g shows the relationship between the number of unpaired electrons and the octahedral distortion (ε), which is consistent with previous reports.[33] The lattice distortion becomes more pronounced with an increase in the number of unpaired spins in $ZnCo_2O_4$. This is because the increased number of unpaired electrons leads to the occupation of e_g orbitals, resulting in a degenerate electronic ground state. This electronic state can induce the Jahn–Teller effect, which lowers the energy and symmetry of the system. Furthermore, FTIR analysis was utilized to investigate the local chemical bond changes in the as-prepared $ZnCo_2O_4$ (Fig. 1h). The absorption bands at 575 cm^{-1} and 670 cm^{-1} correspond to vibrations of the Co–O and Zn–O bond stretching, respectively. As the calcination temperature increases, the peak shapes of the metal–oxygen bonds broaden and shift to higher wavenumbers (Fig. S5†), confirming the emergence of lattice distortion.

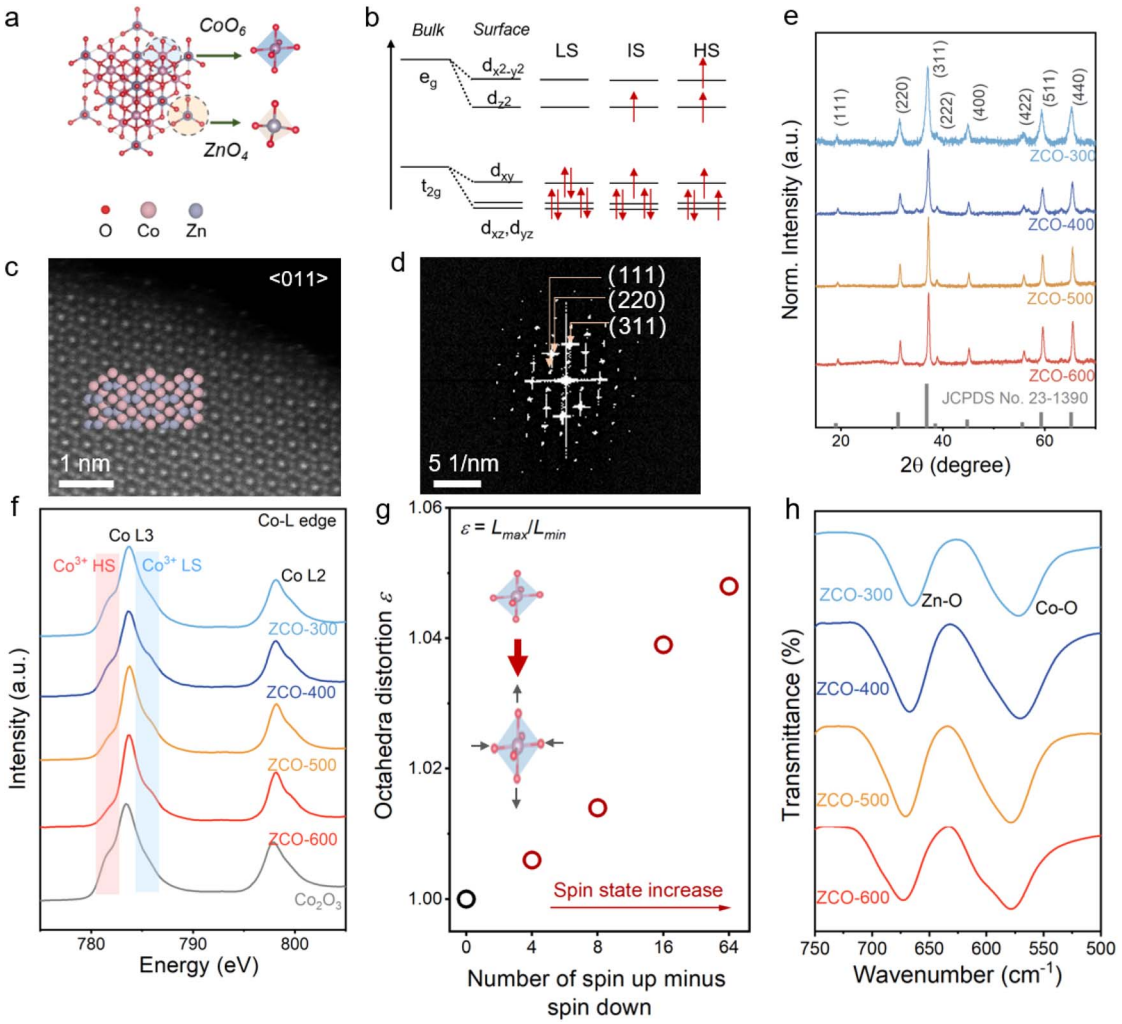

Fig. 1 Structural characterization. (a) Crystal structure of spinel $ZnCo_2O_4$ with Zn^{2+} and Co^{3+} cations occupying tetrahedral and octahedral sites, respectively. (b) d-Electron configurations of the Co^{3+} cation in different spin states in the spinel $ZnCo_2O_4$. (c) AC-HAADF-STEM image of ZCO-600, viewed along the [01$\bar{1}$] zone axis. Theoretical models with octahedral and tetrahedral arrangements are overlaid on the image, with blue and pink atoms representing Zn^{2+} and Co^{3+} cations, respectively. (d) FFT pattern of the TEM image in (c). (e) XRD patterns of the as-prepared spinel $ZnCo_2O_4$ samples, corresponding to the standard pattern PDF# 23-1390. (f)Co $L_{2,3}$-edge XAS spectra of the as-prepared $ZnCo_2O_4$ oxides and Co_2O_3 reference. The red area indicates the Co^{3+} high-spin state peak,[44] and the blue area indicates the Co^{3+} low-spin state peak.[45] (g) Octahedral distortion (ε) associated with an increase in the spin state. The specific computational details are summarized in the ESI.† The inset shows the model changes caused by lattice distortion. (h) FTIR spectra of the as-prepared spinel $ZnCo_2O_4$ oxides.

To gain insights into the spin-related electronic configuration in spinel $ZnCo_2O_4$, the magnetic properties and related spin information were investigated using a SQUID, which consists of a superconducting loop with two parallel Josephson junctions capable of detecting incredibly small changes in magnetic flux.[46] As shown in Fig. 2a, the magnetic properties of the $ZnCo_2O_4$ oxides were investigated by measuring magnetization as a function of the magnetic field (M–H). All the as-prepared $ZnCo_2O_4$ oxides exhibit similar magnetization curves with no hysteresis feature, indicating paramagnetic behavior under ambient conditions. However, the four $ZnCo_2O_4$ oxides exhibit distinct magnetic susceptibilities ($\chi = M/H$), confirming variations in their spin structures.

Temperature-dependent magnetization characterization experiments were carried out to further explore the spin-related properties (Fig. 2b). When the temperature is above 150 K, the magnetic susceptibility of magnetic field induction follows the Curie–Weiss law: $\chi = C/(T-\theta)$, where C is the Curie constant (in emu K mol^{-1} in centimeter-gram-second units) and θ (in K) is the Curie–Weiss temperature.[46] As shown in Fig. 2c, the slope of the fitting curve (susceptibility *vs.* T) represents C^{-1}. The Curie constant C is directly related to the number of unpaired electrons and, once determined, can be used to calculate the effective magnetic moment ($\mu_{eff} = \sqrt{8C}\,\mu_B$, with units of Bohr magnetons, μ_B). Based on recent experimental and theoretical studies, we only consider changes between the low-spin state ($t_{2g}^6e_g^0$) and high-spin state ($t_{2g}^4e_g^2$) without introducing the intermediate-spin state ($t_{2g}^5e_g^1$).[33,47–51] Therefore, the volume fractions of Co^{3+} cations in high-spin and low-spin states can be obtained using the following equation:

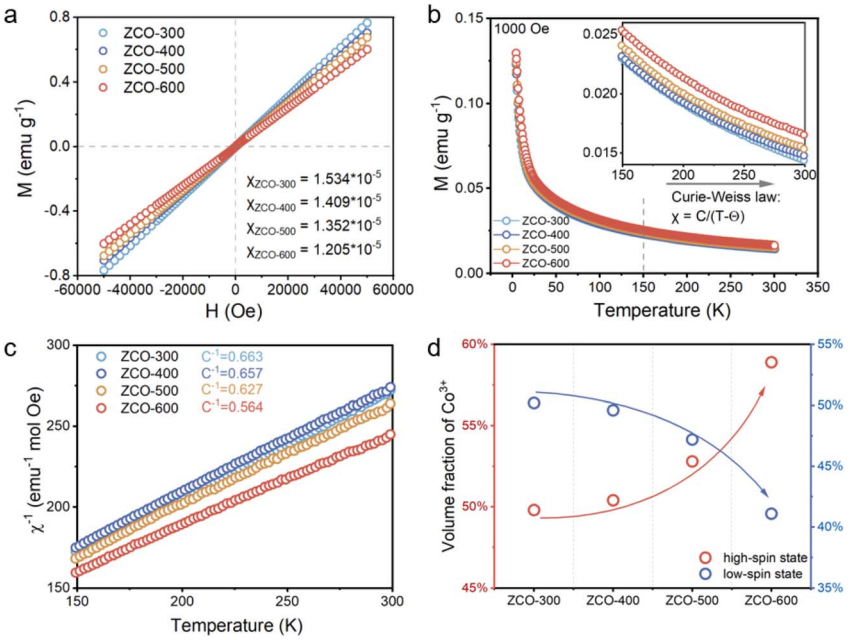

Fig. 2 Spin-related magnetic characterization. (a) Hysteresis loops of the as-prepared $ZnCo_2O_4$ oxides recorded at room temperature (300 K). (b) Temperature-dependent magnetic characterization of the as-prepared $ZnCo_2O_4$ oxides at $H = 1000$ Oe, performed using field-cooling procedures between 5 and 300 K. The inset shows an enlarged view. (c) Fitted susceptibility *versus* temperature based on the Curie–Weiss law for the as-prepared $ZnCo_2O_4$ oxides. (d) Calculated volume fractions of high-spin state and low-spin state Co^{3+} in the four $ZnCo_2O_4$ oxides.

$$\mu_{\text{eff}} = g\mu_B\sqrt{S_{LS}(S_{LS}+1)V_{LS} + S_{HS}(S_{HS}+1)V_{HS}} \quad (1)$$

where S_{LS} ($S_{\text{low-spin}} = 0$) and S_{HS} ($S_{\text{high-spin}} = 2$) are the number of unpaired spins in the e_g orbitals for the low-spin state and high-spin state Co^{3+} cation, respectively; g (=2) is the Landé g-factor. Fig. 2d shows the volume fractions of Co^{3+} in low-spin and high-spin states (more details are displayed in Table S1†). As the calcination temperature increases, the volume fraction of high-spin Co^{3+} increases gradually, indicating that more low-spin Co^{3+} is converted to the high-spin state, thus verifying the success of spin engineering.

After confirming the increase in the high-spin state of the Co^{3+} cation, electrochemical sensing of metal ions was used to explore the intrinsic determinants of metal ion adsorption and desorption affinity on the oxide surface (Fig. 3a). First, the electrochemical impedance spectra (EIS) of $ZnCo_2O_4$ confirmed the enhanced ion transport at the electrode–electrolyte interface in spin-engineered $ZnCo_2O_4$ spinel oxides (Fig. S6†). Then the electrochemical performance of the $ZnCo_2O_4$ oxides was studied using square wave anodic stripping voltammetry (SWASV). Specifically, a 0.1 M HAc–NaAc buffer solution (pH = 6) was employed as the electrolyte, and the deposition process was performed at −1.0 V for 150 s. The electrochemical sensing of metal ions is essentially a surface reaction, where the adsorption and desorption of metal ions occur only on the catalyst surface. Considering that changes in the calcination temperature could affect the specific surface area of the oxides, specific activity is employed to evaluate the electrochemical performance by normalizing the current to the catalyst surface area. In this study, the specific surface area of $ZnCo_2O_4$ oxides was analyzed by N_2 physisorption according to the Brunauer–Emmett–Teller model (Fig. S7†). The electrocatalytic performance of the $ZnCo_2O_4$ spinel oxides toward different metal ions (Cu^{2+}, Cd^{2+}, and Pb^{2+}) is shown in Fig. 3b and S8–S10.† The anodic stripping peaks for Pb^{2+}, Cd^{2+}, and Cu^{2+} ions appear at around −0.55 V, −0.79 V, and −0.05 V respectively, and the peak current increases linearly with the concentration of metal ions. According to the linear equations, the Pb^{2+} electrochemical detection sensitivities of the $ZnCo_2O_4$ oxides are 0.34, 0.575, 0.982 and 1.78 mA cm_{oxide}^{-2} μM^{-1} for ZCO-300, ZCO-400, ZCO-500 and ZCO-600, respectively. And the detection sensitivity of Cd^{2+} and Cu^{2+} ions also gradually improved with increased calcination temperature (more details are displayed in Table S2†). Notably, we found a quasi-linear relationship between the electrochemical performance and the volume fraction of the high-spin state Co^{3+}. As shown in Fig. 3c, sensitivity increases with the volume fraction of the high-spin state Co^{3+}, indicating the significance of the Co^{3+} spin state in electrochemical activity. When we normalized the current to the electrochemically active surface area, we obtained the same trend that the sensitivity increased with the volume fraction of high-spin Co^{3+} (Fig. S11–S13†).

To explore how spin properties affect electrochemical performance, XPS analyses were conducted to reveal the surface chemical interactions between $ZnCo_2O_4$ oxide and *Pb species. As shown in Fig. 3d (top), the characteristic peak of Co 2p shifts to higher energies after adsorption of *Pb species, implying a possible charge transfer from Co to O due to the binding with *Pb species. Additionally, the high-resolution XPS spectra of Pb 4f in $Pb(NO_3)_2$ and ZCO-600/Pb are shown in Fig. 3d (bottom), where the Pb 4f peak shifts toward lower binding energy after adsorption, indicating that the adsorbed *Pb species accept

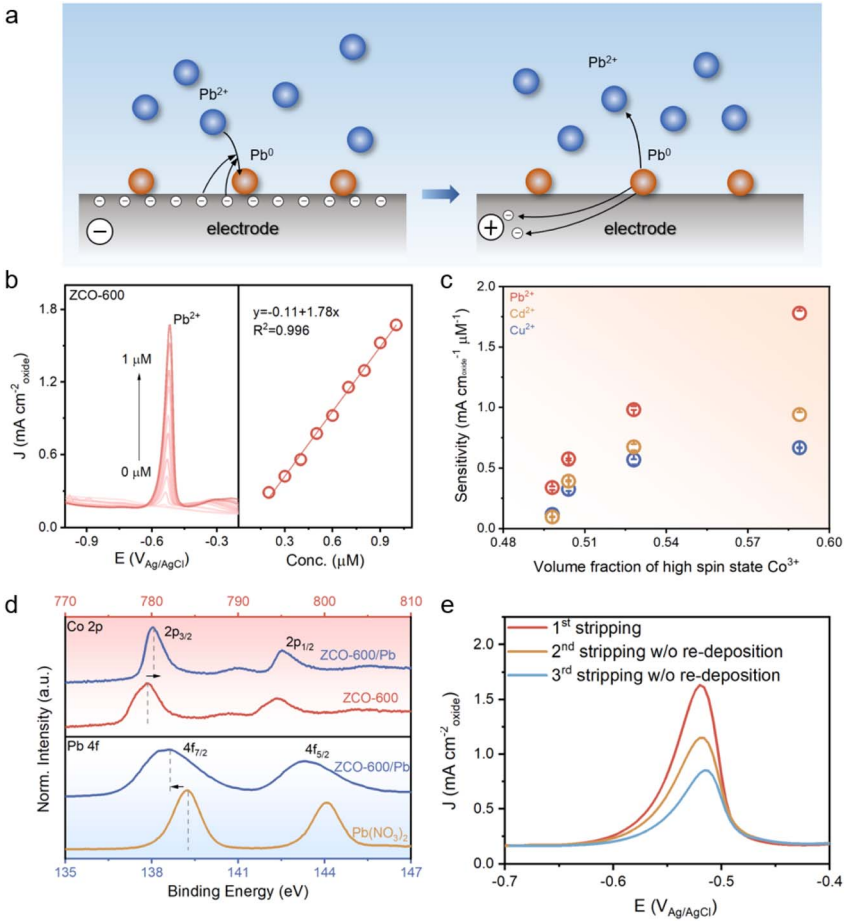

Fig. 3 Electrochemical performance and mechanism. (a) Schematic illustration of the adsorption and desorption processes in electrochemical sensing. (b) SWASV peaks for Pb^{2+} desorption (left) and linear relationship (right) of ZCO-600. (c) Relationship between the volume fraction of high-spin state Co^{3+} and the electrochemical detection sensitivity for Pb^{2+}, Cd^{2+} and Cu^{2+} cations. (d) XPS spectra of Co 2p before and after the adsorption of *Pb species for ZCO-600 (top) and XPS spectra of Pb 4f after the adsorption of *Pb species for ZCO-600 and $Pb(NO_3)_2$ (bottom). (e) SWASV desorption response for 1 μM Pb^{2+} sensing and the 2nd and 3rd anodic stripping curves without re-deposition.

electrons from the oxide. As the high-spin state increases, the Pb 4f peak shifts less toward lower binding energy, indicating that fewer electrons are obtained and the binding force decreases (Fig. S14†). Since electrochemical sensing involves the adsorption and desorption of metal ions at the electrode surface, previous studies predominantly consider a single stripping as the only sensing signal, often overlooking the potential interactions between the metal ion and the electrode.[27] Here, multiple stripping analyses were performed on the adsorbed *Pb species (1 μM). Interestingly, we found that the adsorbed *Pb species cannot be completely stripped in a single cycle (Fig. 3e). As the number of stripping cycles increases, the response current gradually decreases, indicating that the oxide surface still contains unstripped *Pb species after the square wave voltammetry (SWV) process. This confirms that the desorption of metal ions plays a major role in electrochemical sensing performances. These results also suggest that the weaker the binding force between *Pb species and the electrode, the higher the detection performance.

Spin-polarized DFT calculations were further conducted to elucidate the correlation between the Co^{3+} spin state and electrochemical activity (Fig. 4 and S15–S17†). According to the calculated binding energy diagrams of $ZnCo_2O_4$ with varied Co^{3+} spin states (Fig. 4b), the adsorption affinity of metals on $ZnCo_2O_4$ surfaces decreases with the increase of the spin state regardless of the adsorbed metal species (*i.e.*, Pb, Cu and Cd). This is consistent with the experimental electrochemical sensing performances. We further evaluated the projected density of states (PDOS) of the Co 3d orbitals for both low-spin and high-spin states of the $ZnCo_2O_4$ surfaces. As shown in Fig. 4c, the high-spin state exhibits a downshift of the d-band center (−2.01 eV) as compared with that of the low-spin state (−0.92 eV). According to the d-band center theory, it is suggested that lowering the d-band center relative to the Fermi level will weaken the surface chemisorption of adsorbed species, thereby enhancing the electrochemical desorption of metal ions and sensing performances (the d-band center discussed here is the average of the spin-up and spin-down d-band centers). The resulting trend indicates that the spin state alters the electronic properties of the Co sites, leading to a moderate affinity toward the intermediate metal species.

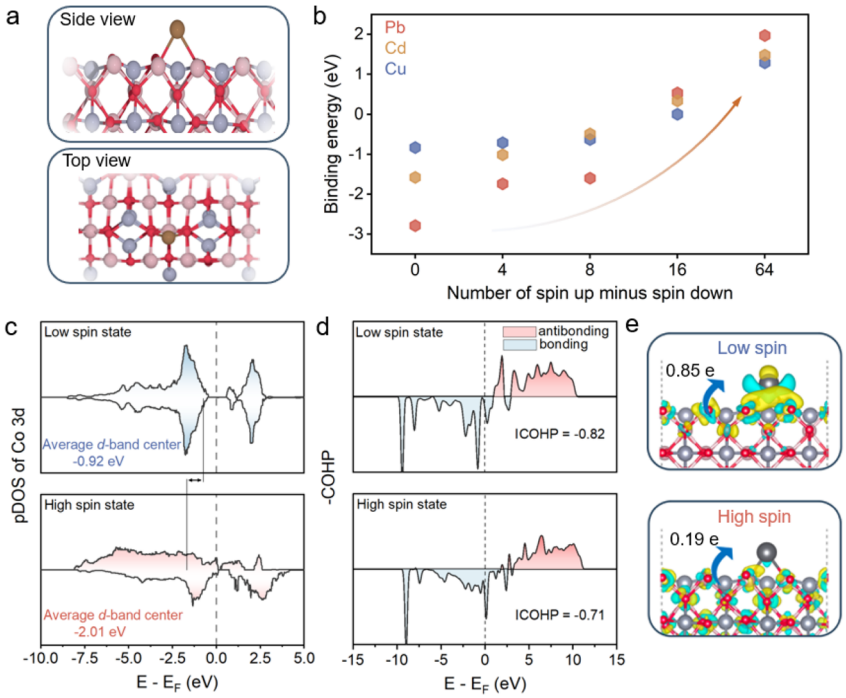

Fig. 4 DFT calculations. (a) Side and top views of the $ZnCo_2O_4$ structure models after the adsorption of *Pb species. Color scheme: Zn, blue; Co, pink; O, red; Pb, brown. (b) Calculated binding energy profiles of different spin state $ZnCo_2O_4$ oxides for *Pb, *Cu and *Cd species. (c) Partial density of states and d-band center of the oxide with both low-spin and high-spin states. (d) COHP for the Co–Pb bond of the low-spin and high-spin state models. (e) Differential charge density and Bader charge analysis of the Pb-adsorbed $ZnCo_2O_4$ surface. The blue areas represent electron depletion, while the yellow areas represent electron accumulation. The isosurface level is set to 0.1 electrons per $Å^3$.

Furthermore, Crystal Orbital Hamilton Population (COHP) analysis was performed to evaluate the binding strength of the Co–Pb interaction after adsorption. The integral area of the COHP (ICOHP) is proportional to the bond strength, with higher electron orbital overlap (lower ICOHP) indicating higher bond strength. Compared to the low-spin state, the high-spin state exhibits decreased occupancy of the bonding state, resulting in a decrease in the -ICOHP (as a measure for the bond strength) of the Co–Pb bond from 0.82 to 0.71 (Fig. 4d), which is consistent with the DFT calculated Co–Pb binding trend. In addition, the charge density difference diagram of both the low-spin state and high-spin state of $ZnCo_2O_4$ structures shows that the charges accumulate on the *Pb species side (yellow region) and deplete on the $ZnCo_2O_4$ side (green region), representing spontaneous electron migration from the Co site to the *Pb species. As illustrated in Fig. 4e, the $ZnCo_2O_4$ structure with the low-spin state transfers more electrons and has stronger adsorption energy than that of the structure with the high-spin state. These results demonstrate the electronic effects under the influence of spin states in $ZnCo_2O_4$ in optimizing the binding strengths of adsorbed metal species.

Conclusions

In summary, we investigated the correlation between the spin state of Co^{3+} sites and their adsorption characteristics with various heavy metal adsorbates. The manipulation of the spin state is achieved using $ZnCo_2O_4$ spinel oxide as a model based on calcination-induced lattice distortion. By using the electrochemical sensing technique as a measure, the adsorption affinity of metal ions on the $ZnCo_2O_4$ surfaces shows a quasi-linear correlation with the volume fraction of high-spin state sites. The high-spin state dominated ZCO-600 shows a Pb^{2+} electrochemical sensing performance of 1.78 mA cm_{oxide}^{-2} μM^{-1}, which is approximately 5-fold higher than that of the low-spin state dominated ZCO-300. Similar spin-based correlations were further demonstrated for various metal species, including Cu^{2+} and Cd^{2+}. DFT calculations show that the d-band center of Co sites gradually shifts downward relative to the Fermi level with the increase of the Co^{3+} spin state in $ZnCo_2O_4$, which weakens the adsorption affinity for metal species. This accounts for the enhanced electrochemical sensing performance toward heavy metal ions. This work unveils the correlation between spin properties and adsorption characteristics of metal species on spinel oxides and points out a potential avenue for the development of next-generation metal-involved technologies, such as sensors, metal batteries and beyond.

Data availability

The data supporting this article have been included as part of the ESI.†

Author contributions

C. G., S. Z. and B. C. designed and carried out the experiments and wrote the manuscript. L. W. collected the TEM data. Y. W.

and Y. C. carried out the electrochemical tests. B. C. and L. Z. supervised the whole study and revised the manuscript. C. G. and S. Z. contributed equally to this work. All the authors discussed the results and commented on the manuscript.

Conflicts of interest

There are no conflicts to declare.

Acknowledgements

This work was supported by the National Natural Science Foundation of China (52201262 and 22373055), the Natural Science Foundation of Shandong Province (ZR2023YQ039 and ZR2022QE001), the Taishan Scholars Program of Shandong Province (tsqn202211042), and the Science and Technology Innovation Committee of Shenzhen Municipality (GJHZ20220913142604008). The authors acknowledge the support from the Tsinghua University Initiative Scientific Research Program, the State Key Laboratory of Intelligent Green Vehicle and Mobility under Project No. ZZ2023-063, and the computation resources from the Tsinghua Center of High-Performance Computing. We acknowledge X-ray magnetic circular dichroism (XMCD) beamline BL12B at the National Synchrotron Radiation Laboratory.

References

1 E. Roduner, *Chem. Soc. Rev.*, 2014, **43**, 8226–8239.
2 C. Vogt and B. M. Weckhuysen, *Nat. Rev. Chem.*, 2022, **6**, 89–111.
3 V. I. Parvulescu, F. Epron, H. Garcia and P. Granger, *Chem. Rev.*, 2022, **122**, 2981–3121.
4 J. Lin, W. Ye, M. Xie, D. H. Seo, J. Luo, Y. Wan and B. Van der Bruggen, *Nat. Rev. Earth Environ.*, 2023, **4**, 785–803.
5 Q. Yun, Y. Ge, Z. Shi, J. Liu, X. Wang, A. Zhang, B. Huang, Y. Yao, Q. Luo, L. Zhai, J. Ge, Y. Peng, C. Gong, M. Zhao, Y. Qin, C. Ma, G. Wang, Q. Wa, X. Zhou, Z. Li, S. Li, W. Zhai, H. Yang, Y. Ren, Y. Wang, L. Li, X. Ruan, Y. Wu, B. Chen, Q. Lu, Z. Lai, Q. He, X. Huang, Y. Chen and H. Zhang, *Chem. Rev.*, 2023, **123**, 13489–13692.
6 M. P. Browne, E. Redondo and M. Pumera, *Chem. Rev.*, 2020, **120**, 2783–2810.
7 C. Xie, Z. Niu, D. Kim, M. Li and P. Yang, *Chem. Rev.*, 2020, **120**, 1184–1249.
8 W. Chang, A. Jain, F. Rezaie and K. Manthiram, *Nat. Catal.*, 2024, **7**, 231–241.
9 S. Sun, Y. Zhang, X. Shi, W. Sun, C. Felser, W. Li and G. Li, *Adv. Mater.*, 2024, 2312524.
10 A. J. Medford, A. Vojvodic, J. S. Hummelshøj, J. Voss, F. Abild-Pedersen, F. Studt, T. Bligaard, A. Nilsson and J. K. Nørskov, *J. Catal.*, 2015, **328**, 36–42.
11 Z. W. Chen, J. Li, P. Ou, J. E. Huang, Z. Wen, L. Chen, X. Yao, G. Cai, C. C. Yang, C. V. Singh and Q. Jiang, *Nat. Commun.*, 2024, **15**, 359.
12 X. Chang, Z.-J. Zhao, Z. Lu, S. Chen, R. Luo, S. Zha, L. Li, G. Sun, C. Pei and J. Gong, *Nat. Nanotechnol.*, 2023, **18**, 611–616.
13 B. Wang and F. Zhang, *Angew. Chem., Int. Ed.*, 2022, **61**, e202111026.
14 B. Hammer and J. K. Norskov, *Nature*, 1995, **376**, 238–240.
15 Z.-J. Zhao, S. Liu, S. Zha, D. Cheng, F. Studt, G. Henkelman and J. Gong, *Nat. Rev. Mater.*, 2019, **4**, 792–804.
16 S. Jiao, X. Fu and H. Huang, *Adv. Funct. Mater.*, 2022, **32**, 2107651.
17 C. Y. Zhang, X. Lu, X. Han, J. Yu, C. Zhang, C. Huang, L. Balcells, A. G. Manjón, J. Jacas Biendicho, J. Li, J. Arbiol, G. Sun, J. Y. Zhou and A. Cabot, *J. Am. Chem. Soc.*, 2023, **145**, 18992–19004.
18 Z. Wang, C. Wang, S. Mao, B. Lu, Y. Chen, X. Zhang, Z. Chen and Y. Wang, *Nat. Commun.*, 2022, **13**, 3561.
19 H. Zhang, J. Gao, D. Raciti and A. S. Hall, *Nat. Catal.*, 2023, **6**, 807–817.
20 Z. Li, Y. Yan, S.-M. Xu, H. Zhou, M. Xu, L. Ma, M. Shao, X. Kong, B. Wang, L. Zheng and H. Duan, *Nat. Commun.*, 2022, **13**, 147.
21 S. Yuan, J. Peng, B. Cai, Z. Huang, A. T. Garcia-Esparza, D. Sokaras, Y. Zhang, L. Giordano, K. Akkiraju, Y. G. Zhu, R. Hübner, X. Zou, Y. Román-Leshkov and Y. Shao-Horn, *Nat. Mater.*, 2022, **21**, 673–680.
22 T. DebRoy, T. Mukherjee, H. L. Wei, J. W. Elmer and J. O. Milewski, *Nat. Rev. Mater.*, 2021, **6**, 48–68.
23 Y. Liang, H. Dong, D. Aurbach and Y. Yao, *Nat. Energy*, 2020, **5**, 646–656.
24 A. M. Abakumov, S. S. Fedotov, E. V. Antipov and J.-M. Tarascon, *Nat. Commun.*, 2020, **11**, 4976.
25 R. Hein, P. D. Beer and J. J. Davis, *Chem. Rev.*, 2020, **120**, 1888–1935.
26 L. Jiao, W. Xu, Y. Wu, H. Wang, L. Hu, W. Gu and C. Zhu, *Anal. Chem.*, 2023, **95**, 433–443.
27 X.-Y. Xiao, Y.-H. Zhao, Y.-Y. Li, Z.-Y. Song, S.-H. Chen, H.-Q. Huang, M. Yang, P.-H. Li and X.-J. Huang, *Anal. Chem.*, 2022, **94**, 13631–13641.
28 S.-M. Lu, Y.-Y. Peng, Y.-L. Ying and Y.-T. Long, *Anal. Chem.*, 2020, **92**, 5621–5644.
29 X. Geng, D. Liu, C. C. Hewa-Rahinduwage, S. L. Brock and L. Luo, *Acc. Chem. Res.*, 2023, **56**, 1087–1096.
30 P. Huang, M. Meng, G. Zhou, P. Wang, W. Wei, H. Li, R. Huang, F. Liu and L. Liu, *Proc. Natl. Acad. Sci. U. S. A.*, 2023, **120**, e2219661120.
31 C.-C. Lin, T.-R. Liu, S.-R. Lin, K. M. Boopathi, C.-H. Chiang, W.-Y. Tzeng, W.-H. C. Chien, H.-S. Hsu, C.-W. Luo, H.-Y. Tsai, H.-A. Chen, P.-C. Kuo, J. Shiue, J.-W. Chiou, W.-F. Pong, C.-C. Chen and C.-W. Chen, *J. Am. Chem. Soc.*, 2022, **144**, 15718–15726.
32 S. Luo, K. Elouarzaki and Z. J. Xu, *Angew. Chem., Int. Ed.*, 2022, **61**, e202203564.
33 Y. Sun, X. Ren, S. Sun, Z. Liu, S. Xi and Z. J. Xu, *Angew. Chem., Int. Ed.*, 2021, **60**, 14536–14544.
34 D. Yi, N. Lu, X. Chen, S. Shen and P. Yu, *J. Phys.: Condens. Matter*, 2017, **29**, 443004.
35 M. A. Halcrow, *Chem. Soc. Rev.*, 2013, **42**, 1784–1795.

36 D. Qian, Y. Hinuma, H. Chen, L.-S. Du, K. J. Carroll, G. Ceder, C. P. Grey and Y. S. Meng, *J. Am. Chem. Soc.*, 2012, **134**, 6096–6099.
37 Y. Zhao, X. Jia, G. Chen, L. Shang, G. I. N. Waterhouse, L.-Z. Wu, C.-H. Tung, D. O'Hare and T. Zhang, *J. Am. Chem. Soc.*, 2016, **138**, 6517–6524.
38 J. Huang, J. Chen, T. Yao, J. He, S. Jiang, Z. Sun, Q. Liu, W. Cheng, F. Hu, Y. Jiang, Z. Pan and S. Wei, *Angew. Chem., Int. Ed.*, 2015, **54**, 8722–8727.
39 S. Zhao, Y. Wang, J. Dong, C.-T. He, H. Yin, P. An, K. Zhao, X. Zhang, C. Gao, L. Zhang, J. Lv, J. Wang, J. Zhang, A. M. Khattak, N. A. Khan, Z. Wei, J. Zhang, S. Liu, H. Zhao and Z. Tang, *Nat. Energy*, 2016, **1**, 16184.
40 G. Yang, J. Zhu, P. Yuan, Y. Hu, G. Qu, B.-A. Lu, X. Xue, H. Yin, W. Cheng, J. Cheng, W. Xu, J. Li, J. Hu, S. Mu and J.-N. Zhang, *Nat. Commun.*, 2021, **12**, 1734.
41 J. Li, M. T. Sougrati, A. Zitolo, J. M. Ablett, I. C. Oğuz, T. Mineva, I. Matanovic, P. Atanassov, Y. Huang, I. Zenyuk, A. Di Cicco, K. Kumar, L. Dubau, F. Maillard, G. Dražić and F. Jaouen, *Nat. Catal.*, 2021, **4**, 10–19.
42 Y. Liu, X. Liu, Z. Lv, R. Liu, L. Li, J. Wang, W. Yang, X. Jiang, X. Feng and B. Wang, *Angew. Chem., Int. Ed.*, 2022, **61**, e202117617.
43 T. Maiyalagan, K. A. Jarvis, S. Therese, P. J. Ferreira and A. Manthiram, *Nat. Commun.*, 2014, **5**, 3949.
44 J.-M. Chen, Y.-Y. Chin, M. Valldor, Z. Hu, J.-M. Lee, S.-C. Haw, N. Hiraoka, H. Ishii, C.-W. Pao, K.-D. Tsuei, J.-F. Lee, H.-J. Lin, L.-Y. Jang, A. Tanaka, C.-T. Chen and L. H. Tjeng, *J. Am. Chem. Soc.*, 2014, **136**, 1514–1519.
45 Z. Hu, H. Wu, M. W. Haverkort, H. H. Hsieh, H. J. Lin, T. Lorenz, J. Baier, A. Reichl, I. Bonn, C. Felser, A. Tanaka, C. T. Chen and L. H. Tjeng, *Phys. Rev. Lett.*, 2004, **92**, 207402.
46 S. Mugiraneza and A. M. Hallas, *Commun. Phys.*, 2022, **5**, 95.
47 M. J. R. Hoch, S. Nellutla, J. van Tol, E. S. Choi, J. Lu, H. Zheng and J. F. Mitchell, *Phys. Rev. B:Condens. Matter Mater. Phys.*, 2009, **79**, 214421.
48 V. Křápek, P. Novák, J. Kuneš, D. Novoselov, D. M. Korotin and V. I. Anisimov, *Phys. Rev. B:Condens. Matter Mater. Phys.*, 2012, **86**, 195104.
49 M. Karolak, M. Izquierdo, S. L. Molodtsov and A. I. Lichtenstein, *Phys. Rev. Lett.*, 2015, **115**, 046401.
50 Y. Duan, S. Sun, S. Xi, X. Ren, Y. Zhou, G. Zhang, H. Yang, Y. Du and Z. J. Xu, *Chem. Mater.*, 2017, **29**, 10534–10541.
51 S. Zhou, X. Miao, X. Zhao, C. Ma, Y. Qiu, Z. Hu, J. Zhao, L. Shi and J. Zeng, *Nat. Commun.*, 2016, **7**, 11510.